RSC Advances

PAPER

View Article Online
View Journal | View Issue

Cite this: *RSC Adv.*, 2017, **7**, 4395

Mechanism of enhancing visible-light photocatalytic activity of $BiVO_4$ *via* hybridization of graphene based on a first-principles study

Yuxuan Chen,[a] Xinguo Ma,*[ab] Di Li,[c] Huihu Wang[b] and Chuyun Huang*[ab]

Received 24th October 2016
Accepted 11th December 2016

DOI: 10.1039/c6ra25721f

www.rsc.org/advances

The interface properties of the hybrid graphene/$BiVO_4$(001) heterojunction were investigated by first-principle calculations incorporating semiempirical dispersion-correction schemes to correctly describe van der Waals interactions. The results indicate that graphene and $BiVO_4$ are in contact and form a stable heterojunction. After equilibration of the graphene/$BiVO_4$ interface, their energy levels are adjusted with the shift of their Fermi levels based on calculated work functions. In addition, electrons in the upper valence band of $BiVO_4$ can be excited to the conduction band under irradiation, and then arrive at the C p_z orbital of graphene, in which the electrons cannot migrate back to $BiVO_4$ and thus are trapped in graphene. Thus, substantial holes are accumulated in the $BiVO_4$(001) surface, facilitating the separation of photogenerated e^-/h^+ pairs. The calculated charge density difference unravels that the charge redistribution drives the interlayer charge transfer from graphene to the $BiVO_4$(001) surface. It is identified that the hybridization between the two components induces an increase of optical absorption of $BiVO_4$ in the visible-light region. A deep understanding of the microcosmic mechanisms of interface interaction and charge transfer in this system would be helpful for fabricating $BiVO_4$-based heterojunction photocatalysts.

Introduction

Bismuth vanadate ($BiVO_4$) is one of the most promising photocatalytic materials for O_2 evolution from water-splitting, and the degradation of organics under visible-light irradiation.[1,2] It is well known that $BiVO_4$ has three main crystalline phases: scheelite-monoclinic (sm-$BiVO_4$), scheelite-tetragonal (st-$BiVO_4$) and zircon-tetragonal (zt-$BiVO_4$).[1] Among them, sm-$BiVO_4$ with a band gap of 2.4 eV and a valence band (VB) edge at approximately 2.5 V *vs.* NHE is the most common phase under ambient conditions and exhibits the highest photocatalytic activity under visible-light irradiation.[3–6] Various successful modifications have been made to improve the photocatalytic and photoelectrochemical activity of $BiVO_4$ using the following techniques: controlling morphologies,[7–9] doping,[10,11] and coupling with metal oxide semiconductors[12,13] or carbon materials.[14] Among the above mentioned strategies, coupling with a different semiconductor or metal to match their energy levels is an effective method to separate charges using internal polarization and charged surfaces, but the importance of these phenomena in $BiVO_4$ have not yet been fully explored.[15,16]

In the reported systems of heterostructured photocatalysts, it is accepted that interface properties of heterojunctions are critical for determining the final photocatalytic activity of the systems.[17–19] Interface properties can be attributed to two important aspects: one is the lattice match between the two components, which is the prerequisite for fabricating heterojunctions; the other is the suitable conduction band (CB) and/or VB levels, considered to be the prime and fundamental requirement for charge transfer and separation in heterostructured interfaces. It is well known that graphene is an electron collector and transporter, and may be used to boost the performance of various energy conversion and storage devices,[20,21] or to be a dispersible carrier for catalysts.[22] The uniqueness of this two-dimensional crystal, *i.e.*, high carrier mobility, make it a dopant with the purpose of manipulating the electronic structure of $BiVO_4$, and thus facilitates the enhancement of the carrier mobility, namely, metal-like electroconductivity.

The graphene/$BiVO_4$ systems successfully prepared *via* a one-step hydrothermal method without the use of any surfactants show superior photoactivity in the degradation of MB, RhB, MO and active black BLG under visible-light irradiation.[14] Considering the large specific surface area, the combination of $BiVO_4$ and graphene effectively inhibits the aggregation of these nanoparticles and consequently gives rise to a higher

[a]*School of Science, Hubei University of Technology, Wuhan 430068, China. E-mail: maxg2013@sohu.com*

[b]*Hubei Collaborative Innovation Center for High-efficiency Utilization of Solar Energy, Hubei University of Technology, Wuhan 430068, China. E-mail: chuyunh@163.com*

[c]*School of Metallurgical Engineering, Xi'an University of Architecture and Technology, Xi'an 710055, China*

photocatalytic performance.[14,23] It is noted that sm-$BiVO_4$ nanoplates (space group: $I2/b$) with exposed (001) facets exhibit greatly enhanced photocatalytic activity[9,24,25] and the rate of oxygen evolution increases with the area of the (001) surface under visible-light irradiation.[24] A higher drift velocity of carriers in the (001) direction would bring more of the majority carrier to the (001) surface and promote reduction.[25] However, compared with the progress in experimental fabrication of graphene/$BiVO_4$(001) heterojunctions, its underlying characteristics of the interaction from a theoretical point of view are still far from being explained. Thus, complementary to previous experimental results, in this work, much effort was made to study the basic mechanisms of interface interaction, charge transfer and separation, and optical properties through density functional theory (DFT) calculations. We finally present a coherent picture of the interface properties, which provides a necessary reference for further optimizing the performance of heterojunctions.

Calculation methods

All calculations were performed using the ultrasoft pseudopotentials (USP) with the exchange and correlation in the Perdew–Burke–Ernzerhof (PBE)[26] and Ceperley–Alder (CA)[27] formalisms of density functional theory as implemented in the CASTEP code. In USP calculations, a pragmatic method to correctly describe van der Waals (vdW) interactions resulting from dynamical correlations between fluctuating charge distributions was taken by the Grimme method.[28] And a hybrid semi-empirical solution from Ortmann, Bechstedt and Schmidt (OBS) was also given to introduce damped atom pair wise dispersion corrections of the form C_6R^{6-} in the DFT formalism.[29] The total energy (E_{total}) is represented as:

$$E_{total} = E_{KS\text{-}DFT} + E_{vdW} \quad (1)$$

where $E_{KS\text{-}DFT}$ is the conventional Kohn–Sham DFT energy and E_{vdW} is the dispersion correction. The semiempirical approach provides the best compromise between the cost of first-principles evaluation of the dispersion terms and the need to improve non-bonding interactions in the standard DFT description. The valence atomic configurations are $6s^26p^3$ for Bi, $3s^23p^63d^34s^2$ for V, $2s^22p^4$ for O, and $2s^22p^2$ for C, respectively. A cutoff energy of 450 eV and a Monkhorst–Pack k-mesh of $3 \times 8 \times 2$ are used.[30] All calculations with the denser meshes ensure that the results are fully converged. Geometry optimizations were done before single point energy calculation, and the self-consistent convergence accuracy was set at 2×10^{-6} eV per atom. The convergence criterion for the maximal force on atoms is 0.03 eV Å^{-1}. The maximum displacement is 2×10^{-4} Å, and the stress is less than 0.03 GPa.

Results and discussion

Structural stability

Before exploring the properties of the graphene/$BiVO_4$ heterojunction, we first investigated the crystal structures of single-layer graphene, bulk $BiVO_4$, and the $BiVO_4$(001) surface. Our optimized lattice parameters for graphene ($a = b = 2.458$ Å, $\alpha = 90.013°$) and bulk $BiVO_4$ (space group: $I2/b$, $a = 5.182$ Å, $b = 5.139$ Å, $c = 11.757$ Å, $\alpha = 89.876°$) are in agreement with experimental values.[31] It is worthwhile to mention that the $I/2b$ space group can be converted to $C2/c$.[15] Since both $I2/b$ and $C2/c$ space groups, which have different unit cell choices and crystallographic axes, are commonly used to describe the scheelite-monoclinic structure of $BiVO_4$, it is necessary to clarify the space group used when referring to specific atomic planes or crystal directions as well as the hkl indices of X-ray diffraction peaks in order to prevent any possible confusion. In fact, it can be inferred clearly that the (001) surface for the $I2/b$ space group is equivalent to the (010) surface for the $C2/c$ space group.[15]

Depending on where the surface is sliced, there are two different structures of the $BiVO_4$(001) surface with the same number of surface dangling bonds (1×1 slab with four dangling bonds), as shown in Fig. 1a. It is well known that the number of ionic layers and the width of vacuum space play crucial roles in the accuracy of the calculations of the atomic relaxation and the electronic properties. A vacuum layer of 10 Å is used to isolate the slab as the boundary condition, which according to other previous work, is good enough to make interactions between neighbouring slabs negligible. Dependence of surface energies on slab thickness presents an oscillating odd–even behavior, as shown in Fig. 1b. The surface energies of slabs with an odd number of layers (model 2) are higher because they have an additional symmetry plane at the slab center, so the atomic displacements on both sides of the slab are mirrored and tend to reinforce each other. It is found that the slabs of the $BiVO_4$(001) surface with an even number of layers (model 1) are energetically more favorable than those with an odd number of layers within the GGA-PBE or LDA-CA formalism. Thus, it can be inferred from Fig. 1 that the ideal 1×1 slab of the $BiVO_4$(001) surface exposes two 2-fold undercoordinated O atoms, a 6-fold undercoordinated Bi atom and a fully 4-fold coordinated V atom. Comparing with our final value of surface energy, the surface energies of the 6-layer slab

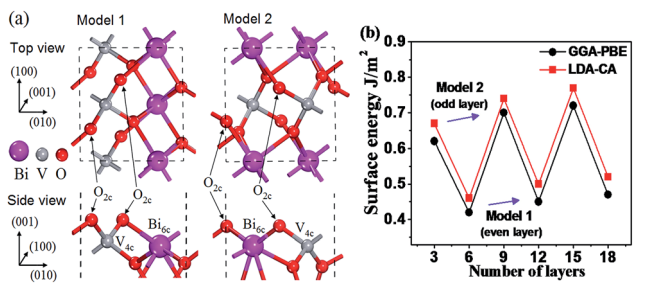

Fig. 1 (a) Top and side views of model 1 (even layer) and model 2 (odd layer) for the $BiVO_4$(001) surface. (b) Surface energies (J m^{-2}) of the $BiVO_4$(001) surface as a function of slab thickness with a 10 Å vacuum within the GGA-PBE and LDA-CA formalism, respectively. Surface energy is defined as follows: $E_{surf} = (E_{slab} - NE_{bulk})/2A$, where E_{slab} and E_{bulk} are the total energies for the slabs (containing N units for the primitive cell) and for the bulk crystal (a primitive cell), respectively; $2A$ is used, as the total area of two equivalent surfaces in the slab model.

only result in an error of −4.5%. So the model of the 6-layer slab is sufficient to present the geometry structure and electronic properties of the $BiVO_4$(001) surface.

To further examine the interaction between graphene and $BiVO_4$(001), based on the TEM and SEM result of graphene/$BiVO_4$ heterojunctions,[32] the graphene/$BiVO_4$(001) interface is modeled by using a supercell slab, in which the geometry structure contains parallel graphene and $BiVO_4$(001) sheets. A 2 × 5 (following the conventional definition of the zigzag/armchair nanoribbon) graphene layer containing 40 carbon atoms was chosen as the substrate to support a 1 × 4 $BiVO_4$(001) surface containing 8Bi, 8V and 32O atoms, as shown in Fig. 2. The whole system contained 88 atoms with 496 valence electrons. The mismatch of initial lattice parameters between the optimized graphene and $BiVO_4$(001) sheets is only 1.6% using the Grimme scheme and 1.8% using the OBS scheme, which are larger than that of the graphene@$MoSe_2$ interface[33] and slightly smaller than that of the graphene@diamond interface.[34] In subsequent work, the Grimme schemes are taken to deal with the vdW interactions in the graphene/$BiVO_4$(001) interface.

To investigate the thermodynamic stability of the graphene/$BiVO_4$(001) heterojunction, the interface adhesion energy was obtained according to the following equation:[33–35]

$$E(\text{ad}) = E(\text{hetero}) - E(\text{graphene}) - E(\text{BiVO}_4(001)) \quad (2)$$

where E(hetero), E(graphene) and E($BiVO_4$(001)) represent the total energies of the relaxed graphene/$BiVO_4$(001) heterojunction, pure graphene, and the pure $BiVO_4$(001) sheet, respectively. The calculated interface adhesion energy of the graphene/$BiVO_4$(001) heterojunction is −16.02 eV (−0.151 eV Å^{-2}), which indicates that the interface is stable. In fact, the interface cohesive energies of the graphene/$BiVO_4$(001) heterojunction contain a lattice mismatch energy, $\Delta E_{\text{mismatch}}$, and other interactions (vdW force) between graphene and the $BiVO_4$(001) surface. Here, the lattice mismatch energy, $\Delta E_{\text{mismatch}}$, of the graphene/$BiVO_4$(001) interface from the strain-driven interaction can be estimated as follows:

$$\Delta E_{\text{mismatch}} = E(\text{BiVO}_4(001))_{a'} + E(\text{graphene})_{a'} - E(\text{BiVO}_4(001))_{\text{a1}} + E(\text{graphene})_{\text{a2}} \quad (3)$$

where $E(\text{BiVO}_4(001))_{a'}$ and $E(\text{graphene})_{a'}$ are the total energies of the isolated $BiVO_4$(001) sheet and isolated graphene with the equilibrium lattice constant a' of the graphene/$BiVO_4$(001) interface, respectively. $E(\text{BiVO}_4(001))_{\text{a1}}$ and $E(\text{graphene})_{\text{a2}}$ represent the total energies of the isolated $BiVO_4$(001) sheet and graphene after all free geometry relaxation, respectively. Our calculated lattice mismatch energy is about −11.37 eV, so the vdW interaction is no more than 4.65 eV (0.044 eV Å^{-2}). After geometric optimization, it is also found that the equilibrium distance between the top of the $BiVO_4$ (001) surface and graphene layer is about 2.99 Å, which is very similar to the results observed for graphene/g-C_3N_4 heterojunctions (3.1 Å).[35] It is nicely matched to the traditional vdW interaction distance, which is a typical vdW equilibrium spacing.[33–35] There is no obvious distortion after geometry optimization, and the shortest distances between the C and Bi/O are 3.034 and 4.019 Å, respectively. It should be noted that when graphene adsorbs onto the $BiVO_4$(001) surface, only physical adsorption occurs; no chemical adsorption is observed. The close but nondestructive contact between graphene and the $BiVO_4$(001) surface may be a unique characteristic for applications as photocatalysts and in solar cells.

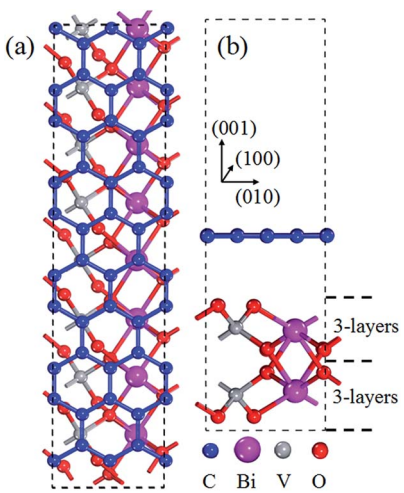

Fig. 2 Top (a) and side (b) views of optimized geometric structures of the graphene/$BiVO_4$(001) heterojunction.

Electronic structure

To understand the effect of the orbital hybridization on electronic structure of the interface, we calculated the energy band structures of the graphene/$BiVO_4$(001) heterojunction using the GGA-PBE method. For the purposes of comparison, the energy bands of isolated graphene, bulk $BiVO_4$ and the $BiVO_4$(001) surface were also calculated. The energy band structures, drawn along high symmetry lines of the Brillouin zone, are shown in Fig. 3. The calculated results show that the graphene is a gapless semiconductor, the (bonding) π bands and (antibonding) π* bands cross only at the corners of the hexagonal Brillouin zone of the system, the so-called K points. A direct band gap of 2.17 eV for bulk $BiVO_4$ is 0.23 eV smaller than the experimental value previously reported by Li *et al.*,[5] due to the well-known limitation in DFT calculations. However, it is noted that the band gap of the $BiVO_4$(001) sheet was calculated to be 2.52 eV, which is very close to the experimental measurement of 2.54 eV using UV-vis absorbance spectroscopy for $BiVO_4$(001) nanoplates.[9]

For the graphene/$BiVO_4$(001) interface, it is found that by comparing Fig. 3a and c, the energy band structures can almost be divided into two groups (from the $BiVO_4$(001) layer or from graphene), due to the weak vdW force between interlayers. This phenomenon is similar to that previously reported by Du *et al.* for a g-C_3N_4/graphene heterobilayer,[35] in which the energy bands near the Fermi level can almost be divided into two groups (from g-C_3N_4 or from graphene) as a result of the relatively weak interlayer coupling. It is noted that the typical

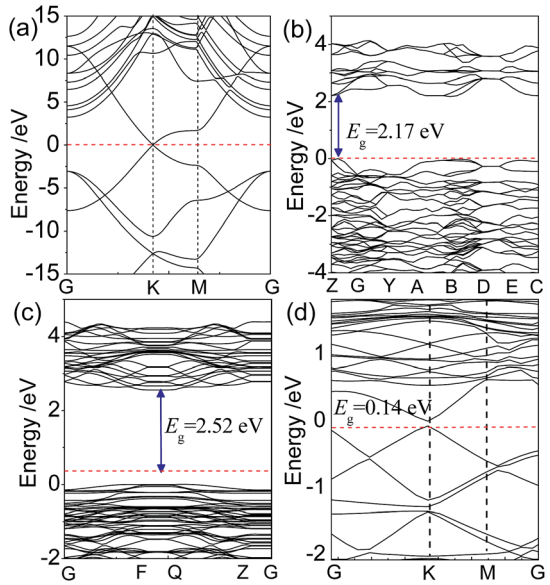

Fig. 3 Calculated energy band structures of (a) graphene, (b) bulk $BiVO_4$, (c) $BiVO_4$(001) sheet, and (d) graphene/$BiVO_4$(001) heterojunction within the GGA-PBE formalism. The Fermi level is set to be 0 eV, indicated by the red dashed line.

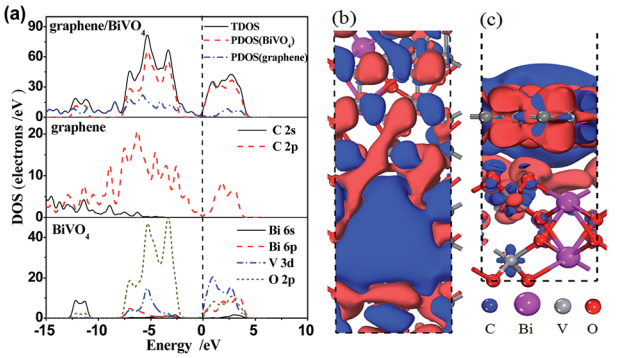

Fig. 4 (a) Calculated total DOS of the graphene/$BiVO_4$(001) heterojunction and PDOS of graphene and $BiVO_4$(001) sheets within the GGA-PBE formalism. The vertical dashed line is the Fermi level. Top (b) and side (c) views of the charge density difference of the graphene/$BiVO_4$(001) interface. Blue and red isosurfaces represent charge accumulation and depletion in the space with respect to isolated $BiVO_4$ and graphene, respectively. The isovalue chosen to plot the isosurface is 0.001 e $Å^{-3}$.

conical structures of the π and π* bands of graphene in the vicinity of the Fermi level are split into double parts (two lines), which is different from those of the isolated graphene. In the graphene/$BiVO_4$(001) interface with the equilibrium interlayer distance d = 2.99 Å, it can be seen that the π and π* linear dispersion bands separate from each other near the Fermi level at the K point, forming a small band gap of 0.14 eV, as shown in Fig. 3d. Thus, graphene adsorbed on the $BiVO_4$(001) surface is no longer a metallic material with massless electrons, but a semiconductor with a direct narrow fundamental band gap. Unfortunately, for the $BiVO_4$–graphene system, the band gap energy is difficult to estimate experimentally from the UV-vis diffuse reflectance spectra data.[14]

Furthermore, we calculated their density of states (DOS) and corresponding partial density of states (PDOS) with the equilibrium interlayer distance d = 2.99 Å between −15 eV and 10 eV, as shown in Fig. 4a. For $BiVO_4$, the VB is composed of hybrid orbitals of Bi 6s and O 2p, whereas the CB is composed of V 3d orbitals.[36] For the graphene/$BiVO_4$(001) heterojunction, the new VB maximum and CB minimum are mainly contributed to by the p_z orbital of the C atoms in the graphene layer. It is noted that the O 2p and V 3d states of the $BiVO_4$(001) layer in the interface extend so that they are neighbouring the Fermi level from the two directions of the VB and CB. Thus, the hybridization between the $BiVO_4$(001) surface and graphene results in a serious decrease of the band gap of $BiVO_4$ in the interface. And the charge transfer is supposed to take place from Bi 6s and O 2p hybrid orbitals to V 3d orbitals upon photoexcitation. As a consequence of this, the introduced states neighbouring the Fermi level greatly enhance the carrier mobility, thus promoting the separation of photogenerated e^-/h^+ pairs.

To further investigate the charge transfer between the $BiVO_4$(001) surface and graphene, the charge density difference was investigated and Milliken analysis was performed to reveal the interlayer charge transfer between graphene and $BiVO_4$. The charge density difference, $\rho_{graphene/BiVO_4(001)} = \rho_{graphene} + \rho_{BiVO_4(001)}$, can be obtained by subtracting the electronic charge of the graphene/$BiVO_4$(001) interface from that of the corresponding isolated graphene and $BiVO_4$(001) surfaces. Fig. 4b and c clearly show that the charge density is redistributed by forming electron-rich and hole-rich regions within the graphene/$BiVO_4$(001) interface. Through Milliken analysis, there is an average charge transfer of 0.04|e| from every top Bi atom to graphene when graphene adsorbs on the $BiVO_4$ (001) surface. In the meantime, the charge transfer of 0.02|e| happens from graphene to every top O atom. This fact implies that the inhomogeneous onsite energy between the interlayers is induced not only by the inhomogeneous charge redistribution between the interlayers caused by graphene, but also by the charge transfer between the $BiVO_4$(001) surface and graphene. As a consequence, the hybridization between graphene and the $BiVO_4$(001) surface disrupts the degeneracy of the π and π* bands of graphene at the K point, resulting in its semiconducting character.

Band edge potentials

To investigate the energy level match between the two components for charge transfer and separation in the heterostructured interface, the band edge energies of the CB and VB of $BiVO_4$ were estimated from the absolute electronegativity of the atoms and the band gap as follows:[37,38]

$$E_C = -\left(\chi(A)^a + \chi(B)^b + \chi(C)^c\right)^{1/(a+b+c)} + \frac{1}{2}E_g + E_0 \quad (4)$$

$$E_V = E_C + E_g \quad (5)$$

where χ(A), χ(B), and χ(C) are the absolute electronegativities of atoms A, B and C, respectively; E_C, E_V and E_g are the band edge energies of the CB and VB and the band gap of semiconductor, respectively; E_0 is the scale factor relating the reference electrode redox level to the absolute vacuum scale (AVS) (E_0 = −4.5 eV for normal hydrogen electrode (NHE)). The average electronegativity, $\chi = (\chi(A)^a + \chi(B)^b + \chi(C)^c)^{1/(a+b+c)}$, of $BiVO_4$ is 6.04. According to eqn (4) and (5), the CB and VB edge potentials of $BiVO_4$ are about 0.34 and 2.74 V *vs.* NHE at pH = pH_{ZPC} (corresponding to that in aqueous solution, the net adsorbed charge of the sample obtained in an electrolyte is zero) with a band gap of 2.4 eV, respectively. It is close to the experimental measurement (0.31 V) carried out using MB solution as a probe material with an initial concentration of 2 mmol dm^{-3}.[39]

The work function of a material is a critical parameter commonly used as an intrinsic reference for band alignment. Here, the work function is calculated and the corresponding energy level lineup diagrams for $BiVO_4$ and graphene before and after equilibrium are plotted, as shown in Fig. 5. The work function is defined as follows:[40]

$$\Phi = E_{vac} - E_F \quad (6)$$

where E_{vac} is the energy of a stationary electron in the vacuum near the surface. E_F is the Fermi level. The calculated electrostatic potentials for graphene, the $BiVO_4$(001) sheet, and the graphene/$BiVO_4$(001) interface are demonstrated in Fig. 5a–c. The calculated work function of $BiVO_4$ (6.68 eV) is larger than that of graphene (4.5 eV). Along with the formation of the graphene/$BiVO_4$ contact, the electrons in graphene with a low work function flow into $BiVO_4$ with a high work function, which thereby levels up the potential energy surface at the interface and eventually builds up an n-type-like Schottky barrier (~0.96 V, see Fig. 5d). As a result, the work function of the graphene/$BiVO_4$ heterojunction is 5.72 eV. It can be inferred that the $BiVO_4$ layer will accumulate negative charges. In the meantime, the graphene layer will gather positive charges. This result is in great agreement with the charge density difference and Mulliken charge analysis.

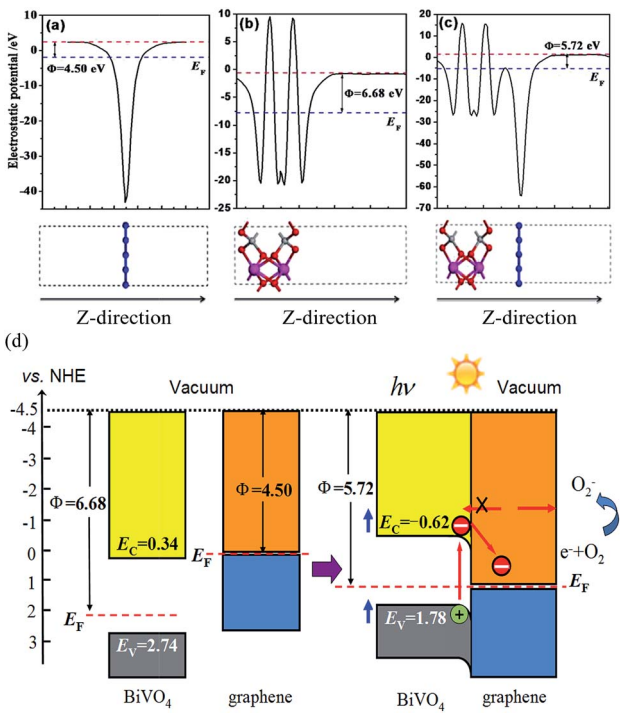

Fig. 5 The electrostatic potentials for (a) graphene, (b) the $BiVO_4$(001) sheet and (c) the graphene/$BiVO_4$(001) heterojunction. The red and blue dashed lines represent the vacuum level, E_0, and the Fermi level, E_F, respectively. (d) Diagram of the band edge positions before and after contact of graphene and $BiVO_4$.

As an n-type photocatalyst, the good hole conductivity of $BiVO_4$ is highly favorable for hole transfer, which is critical for both photocatalytic and photoanodic water oxidation.[15,41] The Fermi level of $BiVO_4$ is located under the CB and is slightly more positive than that of graphene. After equilibration of the graphene/$BiVO_4$(001) interface, the Fermi levels shift in the negative direction for $BiVO_4$ and the positive direction for graphene, respectively, until they are equal. At this time, the CB and VB of $BiVO_4$ are pulled in the negative direction a little, and then form a slightly downward band bending close to the interface between $BiVO_4$ and graphene. It is reasonable to say that under visible-light irradiation, the electrons receiving photon energy in the $BiVO_4$ layer transit from the VB to the CB, then continuously flow into graphene *via* a percolation mechanism,[42] through which the electrons in graphene cannot migrate back to $BiVO_4$ and thus are trapped in graphene. The n-type-like Schottky junction thus boosts the flow of electrons from $BiVO_4$ to graphene and leaves holes in $BiVO_4$, facilitating the separation of photogenerated carriers.[43] In effect, these electrons on the surface of graphene sheets can be captured easily by the adsorbed O_2 molecules to produce superoxide radical anions, $^{\bullet}O_2^-$, because the standard redox potential of $O_2/^{\bullet}O_2^-$ (−0.28 V *vs.* NHE) is more negative than the CB potential of graphene in the interface.[44] In this case, the VB potential (1.77 V *vs.* NHE) of the $BiVO_4$ layer is less positive than the standard redox potential of $^{\bullet}OH/OH^-$ (1.99 V *vs.* NHE), indicating that the photogenerated holes in the VB of the $BiVO_4$ layer could not oxidize OH^- into $^{\bullet}OH$ free radicals with a very strong oxidation capacity. Of course, the VB edge is more positive than the redox potential of RhB (1.43 V).[45] This ascertains, for example, that in the system, direct photogenerated hole oxidation is energetically possible and will photodegrade RhB.[46,47] So the superoxide radical anions, $^{\bullet}O_2^-$, and photogenerated holes are responsible for the degradation of RhB.

Optical absorption

To examine the effect of graphene combination on the photocatalytic efficiency of $BiVO_4$, the optical spectra were investigated by calculating the imaginary part of the complex dielectric function using the GGA-PBE method. It is well known that the allowed transitions are determined by the nonzero matrix elements of the position operator. Here, the optical calculations are achieved using plane polarization with the specified polarization direction where the *E* field vector is parallel to the *x*, *y* or *z* axes (marked as $E\|x$, $E\|y$, $E\|z$) and the "polycrystalline"

polarization where the E field vector is an isotropic average over all directions. In the optical spectra analysis, a small smearing of 0.2 eV is used to greatly distinguish the absorption peaks.

Fig. 6 shows the polycrystalline and polarized optical absorption coefficient spectra of the isolated $BiVO_4$ layer and graphene/$BiVO_4$ interface. For the isolated $BiVO_4$ layer, in the polarization direction of $E||x$ and $E||y$, it is noted that the optical properties are almost the same prominent peaks between 500 and 550 nm, while a different curve is obtained along the polarization direction of $E||z$, as shown in Fig. 6c, which indicates that the $BiVO_4$ layer has strong optical anisotropy. The similarity of the absorption coefficient spectra under $E||x$ and $E||y$ is certainly reasonable since the symmetry of the absorption coefficient spectra corresponds to the symmetry of the lattice structure in the plane directions. In fact, the previous results show clearly that the absorption edge of pure $BiVO_4$, corresponding to the largest wavelength, is about 520 nm, which indicates that $BiVO_4$ is a visible-light semiconductor photocatalyst.[3,47] However, the absorption intensity of pure $BiVO_4$ is so weak in the visible-light region that the optical absorption isn't enough to contribute to the high photocatalytic activity of $BiVO_4$.

It can be seen from the polycrystalline curve of the optical absorption coefficient spectra of the graphene/$BiVO_4$(001) heterojunction in Fig. 6a that the absorption edges extend to more than 950 nm. In addition, Fig. 6b shows that the absorption coefficient spectra of the graphene/$BiVO_4$(001) heterojunction have certain anisotropy in the long wavelength region. By analyzing Fig. 6b, it is found that the two prominent peaks (I and II) in Fig. 6a are mainly contributed to by the absorption coefficient spectra under $E||x$ and $E||y$. It is noteworthy that peak I at 610 nm is mainly contributed to by the effect of the graphene layer on the $BiVO_4$(001) surface, namely, the inhomogeneous charge redistribution between interlayers caused by graphene. Further, it is noted that the absorption coefficient spectrum under $E||x$ has much stronger signals than those under $E||y$ and $E||z$ in the visible-light region, which is attributed to a delocalized electron transition, and is not related to the crystal structure. It is inferred that peak II at 440 nm corresponds to a phototransition energy of about 2.82 eV, from the top of the VB to V 3d levels in the CB of the $BiVO_4$ layer, or Bi 6s and O 2p levels in the VB of the $BiVO_4$ layer to the bottom of the CB. Compared with the results for pure $BiVO_4$, the absorption intensity of the graphene/$BiVO_4$(001) heterojunction increases a lot in the visible-light region due to the large distribution of C 2p states near the new bottom of the CB and the new top of the VB. In fact, Fu *et al.* also reported that the UV-vis diffuse reflectance spectra of pure $BiVO_4$ and $BiVO_4$–graphene photocatalysts show that there is no significant absorption in the region of 520–850 nm for pure $BiVO_4$, while the absorption of $BiVO_4$–graphene is much stronger than that of pure $BiVO_4$ particles covering the whole visible-light region due to the presence of graphene.[14] It is reasonable to consider that the hybridization between $BiVO_4$ layers and graphene induces an increase in the optical absorption range and intensity of $BiVO_4$ in the visible-light region,[14,23,47] and thus their visible-light absorption is enough to contribute to the high photocatalytic activity of heterostructured systems.

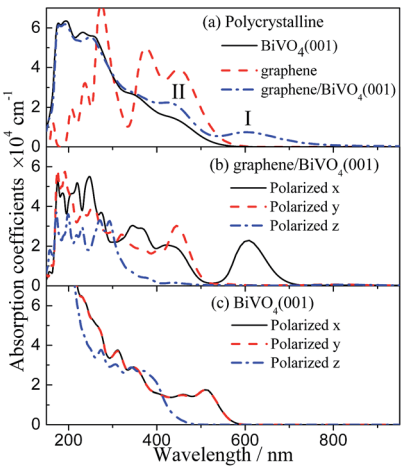

Fig. 6 Calculated polycrystalline and polarized optical absorption coefficient spectra of the graphene/$BiVO_4$ interface and $BiVO_4$(001) sheet.

Conclusions

The microscopic mechanisms of interface interactions, charge transfer and separation, as well as their influence on the photocatalytic activity of graphene/$BiVO_4$(001) heterojunctions have been studied by first-principles calculations incorporating semiempirical dispersion-correction schemes to correctly describe vdW interactions. The mismatch of initial lattice parameters between the optimized graphene and $BiVO_4$(001) layers is only 1.6–1.8%, and the results indicate that the $BiVO_4$(001) surface and graphene are in contact and form a vdW heterostructured interface. By analyzing the energy level based on our calculated work function between the two components, it can be found after equilibration of the graphene/$BiVO_4$(001) interface that the electrons receiving photon energy in the $BiVO_4$(001) layer continuously flow into the C p_z orbital of graphene under visible-light irradiation, in which the electrons cannot migrate back to $BiVO_4$ and thus are trapped in graphene, facilitating the separation of photogenerated carriers. It is further indicated that the hybridization between the two components induces an increase of optical absorption of $BiVO_4$ in the visible-light region. In short, the incorporation of graphene into $BiVO_4$ facilitates the separation of photogenerated e^-/h^+ pairs and the enhancement of visible-light absorption. The present investigation is useful in the wider development of new $BiVO_4$-based heterojunction photocatalysts.

Acknowledgements

This work was supported by the National Natural Science Foundation of China (No. 51472081, 21301135, 51202064), the Foundation for High-Level Talents (GCRC13014), and the Development Funds of Hubei Collaborative Innovation Center (HBSKFMS2014003, HBSKFMS2014011, HBSKFMS2015004).

Notes and references

1 A. Kudo, K. Omori and H. Kato, *J. Am. Chem. Soc.*, 1999, **121**, 11459–11467.
2 K. Shantha and K. B. R. Varma, *Mater. Sci. Eng., B*, 1999, **60**, 66–75.
3 S. Tokunaga, H. Kato and A. Kudo, *Chem. Mater.*, 2001, **13**, 4624–4628.
4 L. Zhang, D. Chen and X. Jiao, *J. Phys. Chem. B*, 2006, **110**, 2668–2673.
5 D. Wang, R. Li, J. Zhu, J. Shi, J. Han, X. Zong and C. Li, *J. Phys. Chem. C*, 2012, **116**, 5082–5089.
6 X. Zhang, Z. Ai, F. Jia, L. Zhang, X. Fan and Z. Zou, *Mater. Chem. Phys.*, 2007, **103**, 162–167.
7 T. W. Kim and K.-S. Choi, *Science*, 2014, **343**, 990–994.
8 Y. Sun, Y. Xie, C. Wu, S. Zhang and S. Jiang, *Nano Res.*, 2010, **3**, 620–631.
9 G. Xi and J. Ye, *Chem. Commun.*, 2010, **46**, 1893–1895.
10 M. Guo, Y. Wang, Q. L. He, W. J. Wang, W. M. Wang, Z. Y. Fu and H. Wang, *RSC Adv.*, 2015, **5**, 58633–58639.
11 D. K. Zhong, S. Choi and D. R. Gamelin, *J. Am. Chem. Soc.*, 2011, **133**, 18370–18377.
12 S. J. Hong, S. Lee, J. S. Jang and J. S. Lee, *Energy Environ. Sci.*, 2011, **4**, 1781–1787.
13 M. Long, W. Cai, J. Cai, B. Zhou, X. Chai and Y. Wu, *J. Phys. Chem. B*, 2006, **110**, 20211–20216.
14 Y. Fu, X. Sun and X. Wang, *Mater. Chem. Phys.*, 2011, **131**, 325–330.
15 Y. Park, K. J. McDonald and K.-S. Choi, *Chem. Soc. Rev.*, 2013, **42**, 2321–2337.
16 J. H. Kim and J. S. Lee, *Energy and Environment Focus*, 2014, **3**, 339–353.
17 J. Jiang, X. Zhang, P. B. Sun and L. Z. Zhang, *J. Phys. Chem. C*, 2011, **115**, 20555–20564.
18 S. C. Yan, S. B. Lv, Z. S. Li and Z. G. Zou, *Dalton Trans.*, 2010, **39**, 1488–1491.
19 L. Ge, C. C. Han and J. Liu, *Appl. Catal., B*, 2011, **100**, 108–109.
20 Z. Liu, Q. Liu, Y. Huang, Y. Ma, S. Yin, X. Zhang, W. Sun and Y. Chen, *Adv. Mater.*, 2008, **20**, 3924–3930.
21 D. Wang, D. Choi, J. Li, Z. Yang, Z. Nie, R. Kou, D. Hu, C. Wang, L. V. Saraf, J. Zhang, I. A. Aksay and J. Liu, *ACS Nano*, 2009, **3**, 907–914.
22 Q. J. Xiang, J. G. Yu and M. Jaroniec, *Chem. Soc. Rev.*, 2012, **41**, 782–796.
23 Y. Sun, B. Qu, Q. Liu, S. Gao, Z. Yan, W. Yan, B. Pan, S. Wei and Y. Xie, *Nanoscale*, 2012, **4**, 3761–3767.
24 D. Wang, H. Jiang, X. Zong, Q. Xu, Y. Ma, G. Li and C. Li, *Chem.–Eur. J.*, 2011, **17**, 1275–1282.
25 R. Munprom, P. A. Salvador and G. S. Rohrer, *J. Mater. Chem. A*, 2015, **3**, 2370–2377.
26 J. P. Perdew, K. Burke and M. Ernzerhof, *Phys. Rev. Lett.*, 1996, **77**, 3865–3868.
27 D. M. Ceperley and B. J. Alder, *Phys. Rev. Lett.*, 1980, **45**, 566–569.
28 S. Grimme, *J. Comput. Chem.*, 2006, **27**, 1787–1799.
29 F. Ortmann, F. Bechstedt and W. G. Schmidt, *Phys. Rev. B: Condens. Matter Mater. Phys.*, 2006, **73**, 205101–205110.
30 H. J. Monkhorst and J. D. Pack, *Phys. Rev. B: Solid State*, 1976, **13**, 5188–5192.
31 A. W. Sleight, H. Chen, Y. A. Ferretti and D. E. Cox, *Mater. Res. Bull.*, 1979, **14**, 1571–1581.
32 J. Zhang, F. Ren, M. Deng and Y. Wang, *Phys. Chem. Chem. Phys.*, 2015, **17**, 10218–10226.
33 Y. D. Ma, Y. Dai, W. Wei, C. W. Niu, L. Yu and B. B. Huang, *J. Phys. Chem. C*, 2011, **115**, 20237–20241.
34 Y. D. Ma, Y. Dai, M. Guo and B. B. Huang, *Phys. Rev. B*, 2012, **85**, 235448–235455.
35 A. J. Du, S. Sanvito, Z. Li, D. W. Wang, Y. Jiao, T. Liao, Q. Sun, Y. H. Ng, Z. H. Zhu, R. Amal and S. C. Smith, *J. Am. Chem. Soc.*, 2012, **134**, 4393–4397.
36 M. Oshikiri, M. Boero, J. Ye, Z. Zou and G. Kido, *J. Chem. Phys.*, 2002, **117**, 7313–7318.
37 Y. Xu and M. A. A. Schoonen, *Am. Mineral.*, 2000, **85**, 543–556.
38 W. J. Chun, A. Ishikawa, H. Fujisawa, T. Takata, J. N. Kondo, M. Hara, M. Kawai, Y. Matsumoto and K. Domen, *J. Phys. Chem. B*, 2003, **107**, 1798–1803.
39 H. Jiang, H. Endo, H. Natori, M. Nagai and K. Kobayashi, *J. Eur. Ceram. Soc.*, 2008, **28**, 2955–2962.
40 R. Garg, N. K. Dutta and N. R. Choudhury, *Nanomaterials*, 2014, **4**, 267–300.
41 Z. Li, W. Luo, M. Zhang, J. Feng and Z. Zou, *Energy Environ. Sci.*, 2013, **6**, 347–370.
42 X. Wang, L. J. Zhi and K. Müllen, *Nano Lett.*, 2008, **8**, 323–327.
43 Y. H. Ng, A. Iwase, A. Kudo and R. Amal, *J. Phys. Chem. Lett.*, 2010, **1**, 2607–2612.
44 T. Berger, D. Monllor-Satoca, M. Jankulovska, T. Lana-Villarreal and R. Gomez, *ChemPhysChem*, 2012, **13**, 2824–2875.
45 T. Shen, Z. G. Zhao, Q. Yu and H. J. Xu, *J. Photochem. Photobiol., A*, 1989, **47**, 203–212.
46 S. B. Gawande and S. R. Thakare, *Int. Nano Lett.*, 2012, **2**, 11–17.
47 Y. Li, Z. Sun, S. Zhu, Y. Liao, Z. Chen and D. Zhang, *Carbon*, 2015, **94**, 599–606.